

# Structure–property relationships in multifunctional thieno(bis)imide-based semiconductors with different sized and shaped *N*-alkyl ends†

Cite this: *J. Mater. Chem. C*, 2014, 2, 3448

Manuela Melucci,<sup>\*a</sup> Margherita Durso,<sup>a</sup> Cristian Bettini,<sup>ab</sup> Massimo Gazzano,<sup>a</sup> Lucia Maini,<sup>c</sup> Stefano Toffanin,<sup>d</sup> Susanna Cavallini,<sup>d</sup> Massimiliano Cavallini,<sup>d</sup> Denis Gentili,<sup>d</sup> Viviana Biondo,<sup>e</sup> Gianluca Generali,<sup>e</sup> Federico Gallino,<sup>f</sup> Raffaella Capelli<sup>d</sup> and Michele Muccini<sup>de</sup>

The relationships between the molecular structure, packing modalities, charge mobility and light emission in organic thin films is a highly debated and controversial issue, with both fundamental and technological implications in the field of organic optoelectronics. Thieno(bis)imide (TBI) based molecular semiconductors provide an interesting combination of good processability, tunable self-assembly, ambipolar charge transport and electroluminescence, and are therefore an ideal test base for fundamental studies on the structure–property correlation in multifunctional molecular systems. Herein, we introduce a new class of thieno(bis)imide quaterthiophenes having alkyl side chains of different shapes (linear, cyclic, branched) and lengths (C1–C8). We found that contrarily to what is generally observed in most molecular semiconductors, the length of the alkyl substituent does not affect the optical, self-assembly and charge transport properties of TBI materials. However, different electroluminescence powers are observed by increasing the alkyl side, this suggesting a potential tool for the selective modulation of TBI functionalities. A deep experimental and theoretical investigation on this new family of TBI materials is provided.

Received 23rd December 2013  
Accepted 23rd February 2014

DOI: 10.1039/c3tc32538e

[www.rsc.org/MaterialsC](http://www.rsc.org/MaterialsC)

## Introduction

Organic semiconductors are subject of intense research for their crucial role as key components of the next generation of electronic devices such as displays, thin-film transistors, solar cells, sensors, and logic circuits.<sup>1</sup> In particular, molecular tailoring and structure–property relationship investigation have allowed significant advances in the device performances, attracting increasing interest from both industry and academia.

In the last few years, the development of a very large library of small molecules and polymeric  $\pi$ -conjugated semiconductors has provided useful design principles for the predefined tailoring of a number of functional properties.<sup>2</sup> P-type semiconductors, both molecular and polymeric,<sup>3</sup> based on different building blocks,<sup>4</sup> have been reported<sup>5</sup> with mobility larger than  $1 \text{ cm}^2 \text{ V}^{-1} \text{ s}^{-1}$  (ref. 6) up to  $17 \text{ cm}^2 \text{ V}^{-1} \text{ s}^{-1}$ .<sup>7</sup> On the other hand, because of both synthetic and technological limits, n-type<sup>8</sup> and ambipolar materials<sup>9</sup> that are crucial for complementary circuits, sensors, and light-emitting transistors (OLETs)<sup>10</sup> have been less documented.<sup>11</sup> Even fewer examples as well as related deep structure–property investigation have been provided for molecular semiconductors showing simultaneous efficient electroluminescence and high mobility ambipolarity.<sup>12</sup> In this context, we recently introduced the class of 2,3-thienoimide (TBI) based oligothiophenes (NTxN) as new multifunctional materials combining good processability, high crystallinity together with ambipolar or n-type charge transport combined to electroluminescence in single layer OLETs. Starting from the first case, namely C4-NT4N (Chart 1),<sup>13</sup> we investigated the effect of the molecular dissymmetry,<sup>14</sup> aromatic  $\pi$ -core type<sup>15</sup> and molecular size<sup>16</sup> on the functional properties of the resulting oligomers.<sup>17</sup>

Alkyl and heteroalkyl end substitution of  $\pi$ -conjugated materials is a widely exploited design strategy to change the solid state organization and packing in thin films, generally resulting in a

<sup>a</sup>Consiglio Nazionale delle Ricerche, Istituto per la Sintesi Organica e la Fotoreattività, (CNR-ISOF), via P. Gobetti 101, 40129 Bologna, Italy. E-mail: manuela.melucci@isof.cnr.it

<sup>b</sup>MIST-ER Laboratory, via P. Gobetti 101, 40129 Bologna, Italy

<sup>c</sup>Dipartimento di Chimica “G. Ciamician”, Università di Bologna, Via F. Selmi 2, 40126 Bologna, Italy

<sup>d</sup>Consiglio Nazionale delle Ricerche, Istituto per lo Studio dei Materiali Nanostrutturati (CNR-ISMN), via P. Gobetti 101, 40129 Bologna, Italy

<sup>e</sup>E.T.C. s.r.l., via P. Gobetti 101, 40129 Bologna, Italy

<sup>f</sup>SAES-GETTERS S. p. A., Viale Italia 77, 20020 Lainate, MI, Italy

† Electronic supplementary information (ESI) available: Synthetic details, optical properties in solution, differential scanning calorimetry, thin deposit morphology and thermal behavior, X-ray diffraction, full electrical characterization, computational details, brightness measurements for C6-NT4N. CCDC 977806. For crystallographic data in CIF or other electronic format see DOI: 10.1039/c3tc32538e

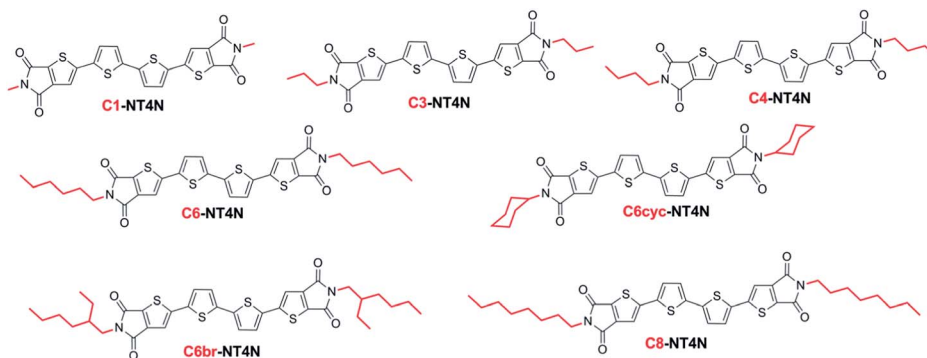


Chart 1 Molecular structure of the compounds herein investigated (C1–C8 linear), C6 branched and cyclic NT4N.

great impact on the charge transport.<sup>4,18</sup> On this basis, aiming at TBI materials with improved electrical performance and at defined property-specific design strategies, here we report a new class of TBI materials having a fixed  $\pi$ -conjugated backbone, length and core type, but differing in the alkyl end substituents.

In particular, TBI molecules, quaterthiophene sized (T4), having linear (C1–C8), branched (C6) or cyclic (C6) alkyl end substituents (Chart 1) have been considered. The optical, thermal, optoelectronic and electrical properties of the newly synthesized materials have been investigated by a combined experimental and theoretical approach and related to the peculiar molecular end motif.

## Experimental

### Synthesis

Compounds **2** and **6** were prepared according to already reported procedures.<sup>13</sup> Compounds **3a–g** are commercially available. The synthesis of the intermediates is reported in the ESI.†

All <sup>1</sup>H, <sup>13</sup>C, NMR spectra were recorded with a Varian Mercury 400 spectrometer operating at 400 MHz (<sup>1</sup>H). Chemical shifts were calibrated using the internal CDCl<sub>3</sub>, acetone-d<sub>6</sub> or CD<sub>2</sub>Cl<sub>2</sub> resonance, which were referenced to as TMS. Mass spectra were collected on an ion trap Thermo scientific ISQ spectrometer operating in electron impact (EI) ionization mode. Melting points were determined by hot stage optical microscopy.

### General procedure for Stille cross-coupling reaction

To a refluxing toluene solution of Pd[(AsPh<sub>3</sub>)<sub>4</sub>] [*in situ*, 6 mol%, Pd<sub>2</sub>(dba)<sub>3</sub> (0.011 mmol), AsPh<sub>3</sub> (0.088 mmol), 5 ml of tol.] and bromo-thieno[3,2-*c*]pyrrole-4,6-dione **5** (0.36 mmol, in 3 ml of toluene), under N<sub>2</sub> atmosphere, commercially available 5,5'-bis(tributylstannyl)-2,2'-bithiophene **6** (0.18 mmol in 2 ml of toluene) was added dropwise. The mixture was refluxed for 48 h then pentane was added at room temperature and the so obtained solid precipitate was purified by flash chromatography on silica gel (CH<sub>2</sub>Cl<sub>2</sub>-petrol. ether = 60 : 40 → CH<sub>2</sub>Cl<sub>2</sub>) and finally by crystallization from toluene.

**2,2'-(2,2'-Bithiophene-5,5'-diyl)bis(5-methyl-5H-thieno[3,2-*c*]pyrrole-4,6-dione), C1-NT4N, 1a.** Dark red powder, 47% yield,

M.p. >350 °C; EI-MS *m/z* 496 (M<sup>+</sup>); UV-vis (CH<sub>2</sub>Cl<sub>2</sub>)  $\lambda_{\max}$  = 451 nm, PL (CH<sub>2</sub>Cl<sub>2</sub>)  $\lambda_{\text{em}}$  = 572 nm ( $\lambda_{\text{exc}}$  = 451 nm). <sup>1</sup>H NMR (CD<sub>2</sub>Cl<sub>2</sub>, TMS/ppm)  $\delta$  7.37 (s, 2H), 7.33 (d, <sup>3</sup>*J* = 3.6 Hz, 2H), 7.25 (d, <sup>3</sup>*J* = 3.6 Hz, 2H), 3.10 (s, 6H). Anal. calcd for C<sub>22</sub>H<sub>12</sub>N<sub>2</sub>O<sub>4</sub>S<sub>4</sub> (496.60): C, 53.21; H, 2.44. Found: C, 53.28; H, 2.97%.

**2,2'-(2,2'-Bithiophene-5,5'-diyl)bis(5-propyl-5H-thieno[3,2-*c*]pyrrole-4,6-dione), C3-NT4N, 1b.** Red orange powder, 80% yield. M.p. 284 °C, MS (70 eV, EI): *m/z* 552 (M<sup>+</sup>), UV-vis (CH<sub>2</sub>Cl<sub>2</sub>)  $\lambda_{\max}$  = 451 nm, PL (CH<sub>2</sub>Cl<sub>2</sub>)  $\lambda_{\text{em}}$  = 572 nm ( $\lambda_{\text{exc}}$  = 451 nm). <sup>1</sup>H NMR (CDCl<sub>3</sub>, TMS/ppm):  $\delta$  7.33 (s, 2H), 7.26 (d, <sup>3</sup>*J* = 3.6 Hz, 2H), 7.18 (d, <sup>3</sup>*J* = 4.0 Hz, 2H), 3.60 (t, 4H), 1.68 (m, 4H), 0.95 (t, 6H). <sup>13</sup>C NMR (CDCl<sub>3</sub>, TMS/ppm):  $\delta$  163.9, 162.7, 149.3, 145.2, 137.8, 137.6, 134.7, 126.8, 125.4, 116.7, 40.2, 22.1, 11.3. Anal. calcd for C<sub>26</sub>H<sub>20</sub>N<sub>2</sub>O<sub>4</sub>S<sub>4</sub>, 56.50; H, 3.65, found: C, 56.70; H, 3.91%.

**2,2'-(2,2'-Bithiophene-5,5'-diyl)bis(5-hexyl-5H-thieno[3,2-*c*]pyrrole-4,6-dione), C6-NT4N, 1d.** Orange powder, 78% yield. M.p. 283 °C, MS (70 eV, EI): *m/z* 636 (M<sup>+</sup>), UV-vis (CH<sub>2</sub>Cl<sub>2</sub>)  $\lambda_{\max}$  = 451 nm, PL (CH<sub>2</sub>Cl<sub>2</sub>)  $\lambda_{\text{em}}$  = 571 nm ( $\lambda_{\text{exc}}$  = 451 nm). <sup>1</sup>H NMR (CDCl<sub>3</sub>, TMS/ppm):  $\delta$  7.32 (s, 2H), 7.26 (d, <sup>3</sup>*J* = 3.6 Hz, 2H), 7.18 (d, <sup>3</sup>*J* = 4 Hz), 3.60 (t, 4H), 1.64 (m, 4H), 1.31 (m, 12H), 0.95 (t, 6H). <sup>13</sup>C NMR (CDCl<sub>3</sub>, TMS/ppm):  $\delta$  163.8, 162.7, 149.3, 145.2, 137.8, 137.6, 134.7, 126.8, 125.4, 116.7, 38.6, 31.4, 28.8, 26.5, 22.5, 14.0. Anal. calcd for C<sub>32</sub>H<sub>32</sub>N<sub>2</sub>O<sub>4</sub>S<sub>4</sub>: C, 60.35; H, 5.06, found: C, 60.39; H, 5.10%.

**2,2'-(2,2'-Bithiophene-5,5'-diyl)bis(5-cyclohexyl-5H-thieno[3,2-*c*]pyrrole-4,6-dione), C6cyc-NT4N, 1e.** Orange powder, 40% yield. M.p. >300 °C, MS (70 eV, EI): *m/z* 632 (M<sup>+</sup>), UV-vis (CH<sub>2</sub>Cl<sub>2</sub>)  $\lambda_{\max}$  = 444 nm, PL (CH<sub>2</sub>Cl<sub>2</sub>)  $\lambda_{\text{em}}$  = 569 nm ( $\lambda_{\text{exc}}$  = 444 nm). <sup>1</sup>H NMR (CDCl<sub>3</sub>, TMS/ppm):  $\delta$  7.31 (s, 2H), 7.25 (d, <sup>3</sup>*J* = 4.0 Hz, 2H), 7.18 (d, <sup>3</sup>*J* = 4.0 Hz), 4.00 (m, 2H), 2.14 (m, 4H), 1.79 (m, 12H), 1.30 (m, 4H). <sup>13</sup>C NMR (CDCl<sub>3</sub>, TMS/ppm):  $\delta$  163.9, 162.7, 149.1, 145.1, 137.7, 126.7, 125.5, 125.3, 116.7, 116.5, 53.4, 51.5, 30.1, 29.7, 26.1, 25.1. Anal. calcd for C<sub>32</sub>H<sub>28</sub>N<sub>2</sub>O<sub>4</sub>S<sub>4</sub>: C, 60.73; H, 4.46, found: C, 60.79; H, 4.50%.

**2,2'-(2,2'-Bithiophene-5,5'-diyl)bis(5-(2-ethylhexyl)-5H-thieno[3,2-*c*]pyrrole-4,6-dione), C6br-NT4N, 1f.** Red-orange solid, M.p. 234 °C, (70 eV, EI): *m/z* 632 (M<sup>+</sup>), UV-vis (CH<sub>2</sub>Cl<sub>2</sub>)  $\lambda_{\max}$  = 451 nm, PL (CH<sub>2</sub>Cl<sub>2</sub>)  $\lambda_{\text{em}}$  = 571 nm ( $\lambda_{\text{exc}}$  = 451 nm). <sup>1</sup>H NMR (CDCl<sub>3</sub>, TMS/ppm):  $\delta$  7.33 (s, 2H), 7.27 (d, <sup>3</sup>*J* = 4.0 Hz, 2H), 7.19 (d, <sup>3</sup>*J* = 4.0 Hz, 2H), 3.55 (t, 4H), 1.92 (m, 2H), 1.35 (m, 16H), 0.95 (m, 12H). <sup>13</sup>C NMR (CDCl<sub>3</sub>, TMS/ppm):  $\delta$  164.1, 162.9, 149.3, 145.2, 137.8, 137.6, 134.7, 126.8, 125.4, 116.7, 42.5, 38.4, 30.5, 28.5,

23.8, 23.0, 14.1, 10.4. Anal. calcd for C<sub>36</sub>H<sub>40</sub>N<sub>2</sub>O<sub>4</sub>S<sub>4</sub>: C, 62.40; H, 5.82, found: C, 62.45; H, 5.89%.

**2,2'-([2,2'-Bithiophene]-5,5'-diyl)bis(5-octyl-4H-thieno[2,3-c]pyrrole-4,6(5H)-dione), C<sub>8</sub>-NT4N, 1g.** Orange powder, 76% yield. M.p. 242 °C, MS (70 eV, EI): *m/z* 692 (M<sup>+</sup>), UV-vis (CH<sub>2</sub>Cl<sub>2</sub>) λ<sub>max</sub> = 450 nm, PL (CH<sub>2</sub>Cl<sub>2</sub>) λ<sub>em</sub> = 568 nm (λ<sub>exc</sub> = 450 nm). <sup>1</sup>H NMR (CDCl<sub>3</sub>, TMS/ppm): δ 7.31 (s, 2H), 7.24 (d, <sup>3</sup>J = 4.0 Hz, 2H), 7.16 (d, <sup>3</sup>J = 3.6 Hz), 3.59 (t, 4H), 1.64 (m, 4H), 1.29 (m, 20H), 0.87 (t, 6H). <sup>13</sup>C NMR (CDCl<sub>3</sub>, TMS/ppm): δ 163.8, 162.6, 149.3, 145.2, 137.8, 137.6, 134.7, 126.8, 125.4, 116.6, 38.6, 31.8, 29.2, 29.1, 28.8, 26.8, 22.6, 14.1. Anal. calcd for C<sub>36</sub>H<sub>40</sub>N<sub>2</sub>O<sub>4</sub>S<sub>4</sub>: C, 62.40; H, 5.82, found: C, 62.43; H, 5.89%.

### Optical spectroscopy

Thin-film UV-visible absorption spectra were recorded with a JASCO V-550 spectrophotometer. Steady-state photoluminescence (PL) was excited using a CW He–Cd laser at 325 nm and collected under transmission conditions (no colour filter was necessary for truncating laser excitation).

PL emission was collected with a calibrated optical multi-channel analyzer (PMA-11, Hamamatsu). Quantum yield measurements of thin-films were carried out by a stand-alone and automatic absolute PL Quantum Yield measurements System (C9920-02, Hamamatsu). The measurements were performed in air and exciting the PL emission at the thin-film absorption maximum wavelength.

### Polarised optical microscopy

Micrographs were recorded with a Nikon i-80 microscope equipped with epi-illuminator, and cross-polars. The thermal treatments of the samples were done using a commercial heating stage (Linkam THMS 600) in air.

### Atomic force microscopy (AFM)

AFM images were recorded with a commercial AFM (Multimode 8, Bruker) operating in semi-contact mode under ambient conditions. Si<sub>3</sub>N<sub>4</sub> cantilevers, with a typical curvature radius of a tip 10 nm, were used. Image analysis was done using the open source SPM software Gwyddion-<http://www.gwyddion.net>.

### Single crystal X-ray diffraction (SC XRD)

Crystal data for C<sub>3</sub>-NT4N were collected on an Oxford Xcalibur S with MoKα radiation, λ = 0.71073 Å, monochromator graphite at room temperature; C<sub>26</sub>H<sub>20</sub>N<sub>2</sub>O<sub>4</sub>S<sub>4</sub>, *M* = 552.68, monoclinic, *a* = 7.4707 (8) Å, *b* = 7.7479 (6) Å, *c* = 43.819 (6) Å, β = 91.54(1)°, *V* = 2535.4(5) Å<sup>3</sup>, space group *C2/c*, *Z* = 4 μ (MoKα) = 0.412 mm<sup>-1</sup>, 5239 reflections measured, 2925 independent reflections (*R*<sub>int</sub> = 0.0332). The final *R*<sub>1</sub> values were 0.0787 (*I* > 2σ(*I*)). The final *wR*(*F*<sup>2</sup>) values were 0.1623 (*I* > 2σ(*I*)). The final *R*<sub>1</sub> values were 0.1124 (all data). The final *wR*(*F*<sup>2</sup>) values were 0.1785 (all data). The goodness of the fit on *F*<sup>2</sup> was 1.167.

### Thin film X-ray diffraction (XRD)

The analysis was carried out by means of a PANalytical X'Pert PRO powder diffractometer equipped with a Ni-filtered Cu Kα

radiation and a fast X'Celerator detector. The data of the devices (powders) have been collected in the 2θ range 2.4–30° (2.4–80°) counting 800 s (200 s) at each step of 0.05° (0.033°).

### OFET/OLET fabrication

The device platform consists of a 420 nm thick PMMA dielectric film, on top of a glass/ITO gate electrode, and gold made drain and source top contact. The PMMA film was spin coated, while the gold electrodes have been evaporated by high vacuum sublimation through a shadow mask process. OLET devices are based on 100 nm thick active organic films, grown by high vacuum sublimation. The channel length (*L*) is equal to 70 μm, while the channel width (*W*) is equal to 12 mm. All opto-electronic measurements were carried out in an MBraun nitrogen glove box using a standard SUSS Probe Station equipped with a Hamamatsu photodiode for light detection.

### Computational details

Molecular and periodic calculations have been performed within spin-polarized DFT, using the hybrid B3LYP functional,<sup>19</sup> as implemented in the CRYSTAL09 code.<sup>20</sup> The all-electron Gaussian-type basis sets adopted were 6-31(d1) for oxygen,<sup>21</sup> nitrogen<sup>22</sup> and carbon,<sup>23</sup> 31(p1) for hydrogen<sup>26</sup> and 8-6311(d1) for sulphur.<sup>24</sup> A post-DFT dispersive contribution, suggested by Grimme,<sup>25</sup> has been added to the computed *ab initio* total energy and gradients in order to account long-range dispersion interactions.

Bulk charge transport has been investigated in the small polaron hopping framework. The intramolecular reorganization energy λ<sub>i</sub> has been computed both within the adiabatic potential (AP) approach and through calculations of Huang–Rhys (HR) parameters.<sup>26</sup> The charge transfer integral τ is evaluated for the nearest neighbouring molecules through the application of Koopmans' theorem in the energy-splitting in the dimer (ESID) model.<sup>27</sup>

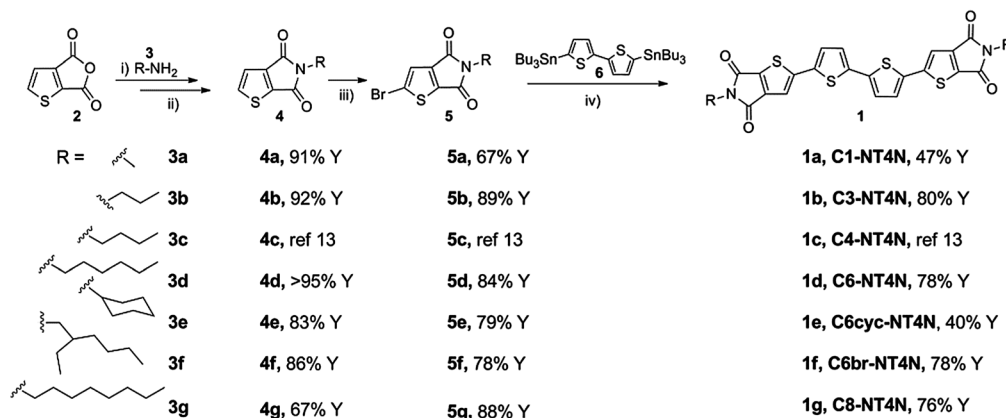
## Results and discussion

### Synthesis

The target compounds in Chart 1 were prepared by conventional Stille coupling reaction by bistannylbithiophene 6 with the proper bromo-TBI (5, Scheme 1). The TBI starting compounds were prepared by ring opening of the thienoanhydride 2 with the alkylamine (3) followed by intramolecular dehydration of the intermediates. The isolated yields ranged from 40% to 80% mainly depending on the final material solubilities. Indeed, methyl and cyclohexyl substituted C1-NT4N and C6cyc-NT4N showed a poor solubility in organic solvents. The solubility increased on increasing the chain size or by using branched substituents.

### Electronic properties

Insights into the electronic properties of the newly synthesized TBI derivatives were obtained by performing optical spectroscopic characterization in diluted solution and thin films.



Scheme 1 Synthetic route to the target compounds. (i) Toluene, reflux, (ii)  $\text{SOCl}_2$  reflux, (iii) TFA,  $\text{H}_2\text{SO}_4$ , NBS, and (iv)  $\text{Pd}(\text{AsPh}_3)_4$ , toluene, reflux. Details in ESI.†

The UV-vis absorption spectra in diluted  $\text{CH}_2\text{Cl}_2$  solutions (see Fig. S1 and Table S1, ESI†) were almost comparable for all the compounds with the maximum absorption wavelength located at about 350 and 450 nm. The emission spectra are featureless with the emission maximum wavelength at around 570 nm.

The absorption spectra of vacuum-sublimed thin-films, reported in Fig. 1, are well structured with absorption maxima located at around 345 and 430 nm for compounds having linear alkyl substituents with  $C > 1$ . **C1-NT4N** was the only compound with the absorption maximum red-shifted to 450 nm. By increasing the alkyl chain length from **C1** to **C8** units no relevant variations in the photoluminescence spectra were observed.

The PL quantum yields ( $\Phi$ , Table 1) measured for the alkyl substituted molecules (from **C1** to **C8**) are almost invariant within the experimental error ranging between 3.5% (**C8-NT4N**) and 6.5% (**C6br-NT4N**).

### Thermal properties

The thermal behaviour of compounds **C1–C8-NT4N** was investigated by combined hot-stage polarized microscopy of thin deposits (POM) and by differential scanning calorimetry (DSC) analyses.

DSC traces show multiple intense temperature transitions beyond the melting one for all compounds with exception for methyl and cyclohexyl ended derivatives **C1-NT4N** and **C6cyc-NT4N** respectively, revealing liquid crystalline properties for these compounds (Table 2).

The thermograms of compound **C8-NT4N** taken as model systems are depicted in Fig. 2, while those of the other compounds are reported as ESI (Fig. S2†). Accordingly to DSC, hot-stage POM revealed LC properties for compounds **C3–C8-NT4N** while only thermal decomposition was observed for **C1-NT4N**. The transition temperatures and the melting enthalpies are listed in Table 2.

### Thin deposits

The thin deposits of compounds **C1–C8-NT4N** for POM analysis were prepared by drop casting a chloroform solution (30  $\mu\text{l}$ ) of

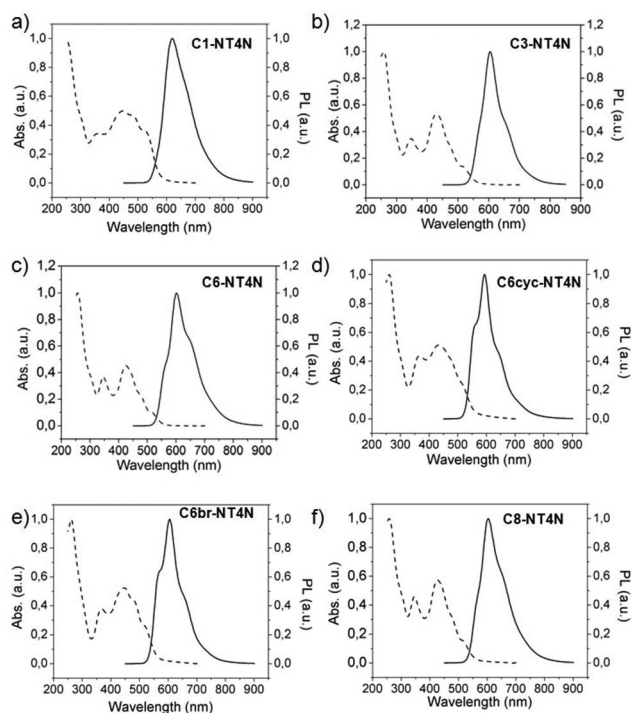


Fig. 1 (a–f) UV-vis and PL spectra vacuum-sublimed thin-films of all compounds (the spectra of **C4-NT4N** are reported in Fig. S1, ESI†).

Table 1 Spectroscopic parameters of thin films of 100 nm thick NT4N derivatives

Item	$\lambda_{\text{abs}}$ (nm)	$\lambda_{\text{em}}^a$ (nm)	$\Phi^b$ (%)
<b>C1-NT4N</b>	350, 450	617	4
<b>C3-NT4N</b>	345, 429	605	6
<b>C4-NT4N</b>	345, 430	603	5
<b>C6-NT4N</b>	346, 426	602	5
<b>C6cyc-NT4N</b>	365, 432	592	4
<b>C6br-NT4N</b>	368, 446	604	6.5
<b>C8-NT4N</b>	345, 427	604	3.5

<sup>a</sup>  $\lambda_{\text{exc}} = 325$  nm. <sup>b</sup> Excitation at absorption maximum.

Table 2 Thermal properties of compounds C1–C8-NT4N. For compound C4-NT4N see ref. 13

Compound	Transition temperature [°C] (melting enthalpies [J g <sup>-1</sup> ])	
	Heating (20°C min <sup>-1</sup> )	Cooling (20°C min <sup>-1</sup> )
1a, C1-NT4N <sup>a</sup>	Nd	Nd
1b, C3-NT4N	274 (3.0), 289 (73.4), 301 (1.1)	262 (55.2), 281 (1.0)
1d, C6-NT4N	244 (1.5), 265 (21.3), 287 (5.9)	219 (0.8), 243 (21.4), 269 (4.9)
1e, C6cyc-NT4N	344 (1.8), 367 (73.9)	329 (15.1)
1f, C6br-NT4N	218 (1.1), 235 (26.1)	213 (29.4), 201 (0.6)
1g, C8-NT4N	121 (2.7), 248 (40.5), 279 (12.1)	231 (41.9), 266 (11.9)

<sup>a</sup> No transitions were observed up to 400 °C.

1 g l<sup>-1</sup> or saturated solution) on quartz slides in a saturated atmosphere of solvent vapours.

All thin deposits exhibit similar morphologies,<sup>28</sup> the material tends to accumulate at the boundaries of the drop because of the inhomogeneous evaporation of the solvent during the shrinking.<sup>29</sup> Larger crystals (size >100 μm) whose shape depended on the molecular structure, accumulate at the boundaries while towards the centre of the droplet their sizes decrease till a few μm; furthermore, in the case of compounds C3-, C6- and C8-NT4N a continuous film in between the crystals was observed by atomic force microscopy (AFM) and POM.

As a representative case, compound C8-NT4N is herein discussed while details on POM analysis of all the other compounds are reported in the ESI (Fig. S3†).

When deposited on glass C8-NT4N forms a continuous film on the surface whose thickness increases from the centre to the boundaries. Under POM, the film exhibits birefringence without extinguishing at any direction (Fig. 3a). Furthermore in the centre of the deposit birefringent fiber-like crystals were often observed (Fig. 3b). The fiber-like crystals appear as long crystallites (>50 μm) randomly distributed on the surface, with width ranging from 200 nm to 10 μm resulting in an aspect ratio (length–width) between 1 : 5 and >1 : 10. The fibers exhibit a strong birefringence, however they do not extinguish at any directions, indicating a polycrystalline nature. In good accordance with the DSC trace (Fig. 2), C8-NT4N thin deposits show a transition to the LC phase at 255 °C followed by the transition to the isotropic phase at 280 °C. By heating above 255 °C, C8-NT4N

became a liquid crystal and de-wets forming a homogeneous distribution of droplets which exhibit the typical behaviour of a smectic liquid crystal (Fig. 3c). Accordingly, atomic force microscopy (AFM) investigation revealed crystals with well defined borders and angles and very slight roughness terraces (r.m.s. roughness <1 nm).

### XRD of single crystal, powder, thin films

Compound C3-NT4N afforded single crystals useful for crystal structure solution and molecular packing determination. The molecule is centrosymmetric and the backbone is almost planar being the two inner thiophene rings strictly coplanar and the dihedral angle between the thiophene and the thiophene-imide units 1.1(4)° (Fig. 4a). Differently from what observed for C4-NT4N in previously reported study,<sup>13</sup> the thiophene-imide units are in uncommon *syn* conformations.<sup>30</sup> The π-conjugated backbones of compound C3-NT4N of adjacent molecules run parallel to one another with an interlayer distance of ca. 3.54 Å as observed also in the recently reported structure of C4-NT4N.<sup>13</sup> The molecules are involved in a bifurcated C–H···O hydrogen

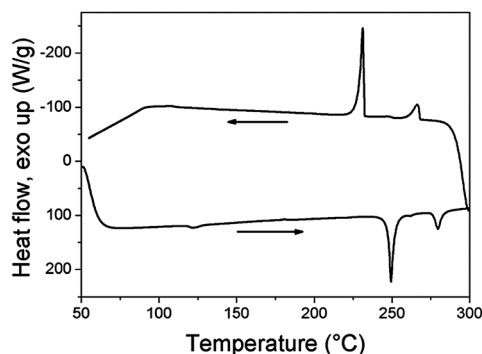


Fig. 2 DSC traces (second heating and cooling steps) at 20°C min<sup>-1</sup> of compound C8-NT4N.

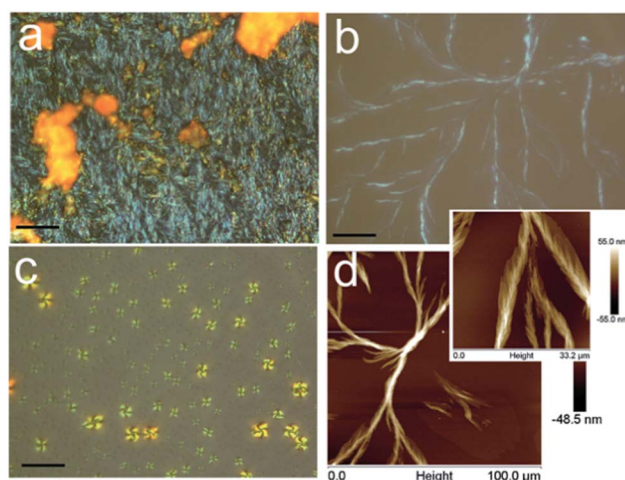


Fig. 3 Optical micrographs taken by POM (cross-polars are oriented parallel and perpendicular to the axis of the images) and the AFM image of C8-NT4N thin deposits. (a) Birefringent continuous film at the boundary of the deposit. Bar length 100 μm. (b) Fiber like crystals at the centre of deposit. Bar length 10 μm. (c) LC phase at 260 °C. Bar is 100 μm. (d) AFM image of (b).

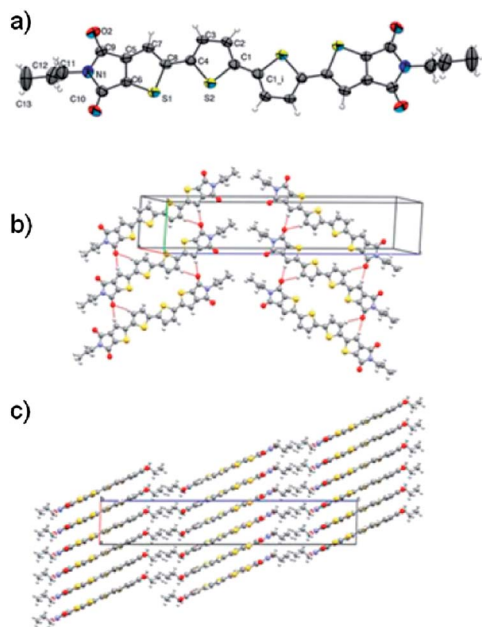


Fig. 4 (a) ORTEP drawing of C3-NT4N (displacement ellipsoids drawn at the 50% probability level). Unlabeled atoms are related to the labelled atoms by symmetry operation  $1/2 - x, 1/2 - y, -z$ . (b) Arbitrary units of the crystal packing showing the C–H–O interactions (red lines). (c) View along the *b* axis showing the  $\pi$ -stack interactions and the assembly of the layers.

bond to form a 1D network (Fig. 4b). The  $\pi$ -stack and hydrogen bond interactions pack efficiently the molecules to form layers having in the inner part the conjugated backbone and the alkyl chains on the surfaces, these layers pile up along the long axis (Fig. 4c). The XRD pattern calculated from the structural data fits very well with that experimentally collected for the C3-NT4N powder sample confirming that the crystal phase is the same (Fig. S4, ESI†). No significant differences are observed for the other compounds showing XRD patterns of the powder reminiscent of that of C3-NT4N with an intense peak at a low angle which suggests the presence of a long axis.<sup>31</sup>

The XRD plots of vacuum evaporated films on the PMMA substrate for compounds C4–C8-NT4N are shown in Fig. 5a. The high intensity in the 0 0 1 reflections of the C3-NT3N device reveals the presence of a strong preferential orientation of the molecules with respect to the substrate in the film. The profiles are very similar to one another differing in the position of the main reflections. Indeed each profile shows two or more intense and sharp reflections that are further orders of the interlayer distance reported in the inset of Fig. 5a.

The value of the distance progressively increases on increasing the length of the alkyl chain. Based on the preferential orientation parameter obtained from C3-NT3N, for which the single crystal structure is known, the sketch of the molecular organization in thin films is depicted in Fig. 5b.

The molecules are arranged in the upright position with respect to the substrate with a minimal interdigitation of the alkyl ends.

Due to the strict similarity of the XRD patterns and to the trend of the interlayer distance with the alkyl chain length, we

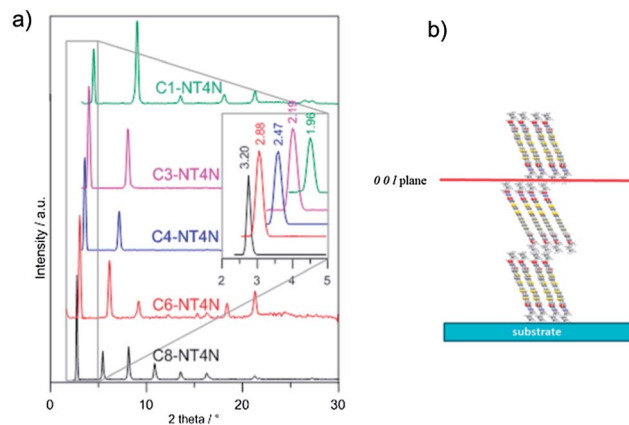


Fig. 5 (a) XRD patterns of compounds C1, C3, C4, C6, C8-NT4N devices directly exposed to the X-ray beam. In the inset the small angle region is enlarged and the corresponding interlayer distances are reported in nm. (b) Schematic representation of the C4-NT4N molecule arrangement on the substrate.

can reasonably assume that all the investigated C1–C8-NT4N molecules adopt a similar upright molecular arrangement.

### Electrical characterization

Electrical characterization of compounds in Chart 1 was performed in a top contact device configuration (details in the Experimental section). The representative transfer and multiple output (*n*-type) electrical curves of compounds C1 and C8-NT4N are shown in Fig. 6 and Table 3 summarizes the charge transport and electroluminescence data expressed as device emission power. Considering the electrical properties, it can be noted that contrarily to conventional oligothiophenes, for which cyclohexyl end substitution promotes charge transport,<sup>23</sup>

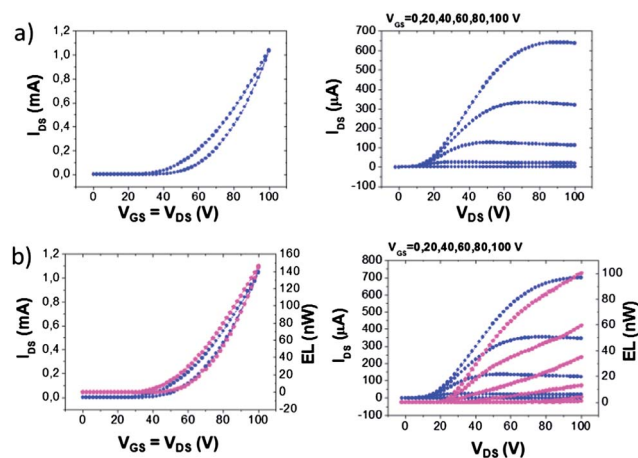


Fig. 6 Left, *n*-type locus curves, right, *n*-type multiple output curves for compounds C1 and C8-NT4N (a and b, respectively). In each graph, the blue dotted curves represent the device drain–source current (referred to the left scale), while the purple dotted curves represent the emitted optical power (referred to the right scale). The *p*(*n*)-type locus curves, multiple output and saturation transfer curves for all compounds are reported in the ESI.†

**Table 3** Electrical parameters for compounds in Chart 1 measured under the same experimental conditions. Film thickness 100 nm

Compound	$\mu_e$ [cm <sup>2</sup> V <sup>-1</sup> s <sup>-1</sup> ]	$\mu_h$ [cm <sup>2</sup> V <sup>-1</sup> s <sup>-1</sup> ]	$V_T^N/V$	$V_T^P/V$	EP [nW]
<b>C1-NT4N</b>	$3.0 \times 10^{-1}$	$2.8 \times 10^{-3}$	27	-61	nd
<b>C3-NT4N</b>	$2.4 \times 10^{-1}$	$1.5 \times 10^{-4}$	40	-45	30
<b>C4-NT4N</b>	$2.9 \times 10^{-1}$	$8.0 \times 10^{-5}$	33	-70	47
<b>C6-NT4N</b>	$1.7 \times 10^{-1}$	$1.3 \times 10^{-4}$	20	-66	145
<b>C8-NT4N</b>	$3.2 \times 10^{-1}$	$3.0 \times 10^{-3}$	28	-62	150
<b>C6cyc-NT4N</b>	$2.9 \times 10^{-2}$	Nd	40	Nd	Nd
<b>C6br-NT4N</b>	Nd	Nd	Nd	Nd	Nd

**C6cyc-NT4N** shows lower electrical performances (Fig. S6, ESI†). Similarly, the branched **C6**-tail does not promote either charge transport or EL. On the other hand, linear alkyl tail compounds (**C1**–**C8-NT4N**) show ambipolar behaviour with a major n-type contribution to charge transport. The hole mobility,  $\mu_h$ , covers a wide range of values, oscillating between 2 and 3.5 orders of magnitude lower than electron mobility  $\mu_e$  that ranges between 1.7 and  $3.2 \times 10^{-1}$  cm<sup>2</sup> V<sup>-1</sup> s<sup>-1</sup>. The observed major electron charge transport was investigated by theoretical calculations in the framework of the small polaron hopping model.<sup>23</sup> A thorough understanding of the correlation between the molecular structure and charge mobility is provided by the investigation of the inner reorganization energy  $\lambda_i$  and the charge transfer integral  $\tau$ . The former is an intrinsic molecular property, packing independent, while the latter represents the electronic coupling element between neighbouring molecules and therefore critically depends on the order in the solid state. Only minor differences in  $\lambda_i$  are observed by varying the alkyl-substituent type and/or length, with all the values included in a 30–40 meV width range (see Table S3†). Moreover, the slight promotion of p-type transport in terms of  $\lambda_i$  (*i.e.*  $\lambda_{ih} < \lambda_{ie}$ ) is in strong disagreement with the measured FET mobilities (Table 3).

Therefore, the predominance of n-type behaviour cannot be understood at a molecular structure level but requires also the analysis of the molecular packing. Consequently, the transfer integrals of **C3-NT4N**, for which the crystal structure was determined (and the XRD show comparable thin film crystal packing), were calculated to gain an insight into the packing-charge transport relationships. The possible charge hopping pathways are shown in Fig. 7.

As shown from data in Table 4, the highest electronic couplings are computed for the dimers involving first next-neighbouring molecule pairs, namely pathways 1, 2 and 3. The latter shows not negligible electron transfer integral values,  $\tau_e$  while only one pathway, namely pathway 1, has a significant hole transfer integral  $\tau_h$ . All the directions are, therefore, favourable for electron transport (*i.e.*  $\mu_e$ ) while only one allows the hole transport (*i.e.*  $\mu_h$ ).

In Table 5 bulk charge mobilities, computed in the non-adiabatic hopping model  $\mu_{\text{calc}}$  (see ESI† for details), have been reported for a comparison with the experimental FET ones,  $\mu_{\text{FET}}$ .

The electron mobility shows a good agreement with experiments, while the hole mobility dramatically overestimates the

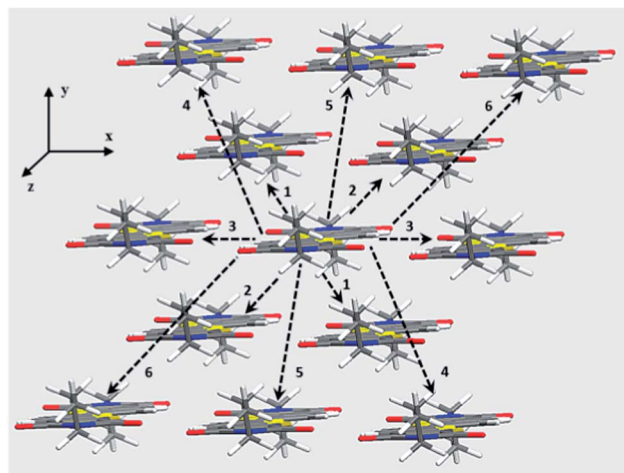


**Fig. 7** Charge hopping pathway schemes for molecule **C3-NT4N** in the bulk crystal. *y* and *z* axis perpendicular and parallel to the molecular axis, respectively.

**Table 4** Computed charge transfer integrals  $\tau$  for all the pathways having distances lower than 11 Å for molecule **C3-NT4N**. Displacements between molecules reported by *r*

Pathway	<i>r</i> [Å]	$\tau_h$ [meV]	$\tau_e$ [meV]
1	5.38	51.56	46.72
2	5.38	7.48	74.86
3	7.75	3.13	26.26
4	10.76	0	0.39
5	7.47	0.14	0.97
6	10.76	0.41	0.15

FET one of about three order of magnitudes. This discrepancy may be ascribed to the different types of computed and experimental mobility. At the theory level, the charge mobility is described by Brownian motion of charge carriers with no spatial constraints, while the experimental FET mobility strictly depends on the source–drain potential tensor that means the device configuration (*e.g.* film orientation). In this sense, while electrons can move along any crystal directions thanks to non-negligible transfer integrals  $\tau$ , hole transport is significantly high only along one pathway (see Table 4). If the latter is forbidden by device configuration, even a damping of some orders of magnitude may become possible for  $\mu_h$ . Thus, by ignoring the pathway 1, we get  $\mu_{\text{calc},e}^* = 2.13 \times 10^{-1}$  cm<sup>2</sup> V<sup>-1</sup> s<sup>-1</sup> and  $\mu_{\text{calc},h}^* = 2.20 \times 10^{-3}$  cm<sup>2</sup> V<sup>-1</sup> s<sup>-1</sup>, in much better agreement with the experimental FET mobility.

**Table 5** Charge mobilities for molecule **C3-NT4N**: experimental FET mobility  $\mu_{\text{FET}}$  and computed bulk mobilities  $\mu_{\text{calc}}$  and  $\mu_{\text{calc}}^*$  obtained by considering all the pathways reported in Fig. 7 and excluding pathway 1, respectively

	$\mu_{\text{FET}}$ [cm <sup>2</sup> V <sup>-1</sup> s <sup>-1</sup> ]	$\mu_{\text{calc}}$ [cm <sup>2</sup> V <sup>-1</sup> s <sup>-1</sup> ]	$\mu_{\text{calc}}^*$ [cm <sup>2</sup> V <sup>-1</sup> s <sup>-1</sup> ]
Hole	$1.5 \times 10^{-4}$	$1.15 \times 10^{-1}$	$2.20 \times 10^{-3}$
Electron	$2.4 \times 10^{-1}$	$1.82 \times 10^{-1}$	$2.13 \times 10^{-1}$

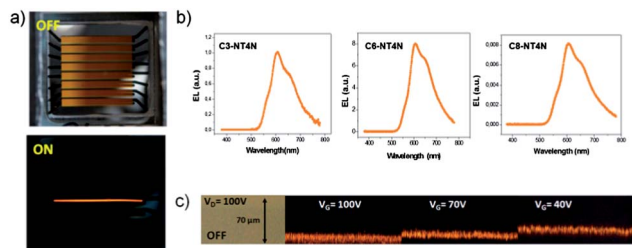


Fig. 8 (a) Images of a device in the OFF state and in the ON state showing light emission visible by eyes. (b) Electroluminescence spectra of compounds C3, C6, and C8-NT4N. (c) Optical imaging of the emissive stripe motion in the channel achieved by tuning the gate voltage for compound C6-NT4N.

As shown by the curves in Fig. 6 (Fig. S8, ESI<sup>†</sup>) and data in Table 3, the emission power signal of the device (taken as comparative parameter) slightly increases on increasing the tail length from C3 to C8. Being the thin films quantum yields almost comparable for all compounds, further investigation to understand the exciton generation and decay processes within the organic electroluminescent transistor device will be carried out. The EL spectra of compounds C3, C6, C8-NT4N are shown in Fig. 8b and are similar to the PL ones (Fig. 1b, c and f) demonstrating that the EL emission truly comes from the organic active layer. Fig. 8c shows the movement of the emissive stripe inside the device channel by changing the applied bias, a typical feature of ambipolar OLETs also previously observed for other TBI materials including C4-NT4N.<sup>14</sup>

## Conclusions

In summary, we investigated the effect of the *N*-alkyl end shape and size on the optical, self-assembly and charge transport properties of a new rational family of thieno(bis)imide based materials. Contrarily to what generally observed for conventional oligothiophenes, no significant effects on the optical properties, thin films morphology and charge mobility resulted from the different structural end-motifs. Major electron charge transport with mobility up to  $0.3 \text{ cm}^2 \text{ V}^{-1} \text{ s}^{-1}$  was measured in OFET configuration, and rationalized by theoretical calculations. Tail dependent electroluminescence was also observed suggesting the potential key role of the *N*-alkyl end of the TBI moiety for the selective modulation of the electroluminescence of these materials for ambipolar single layer OLET device applications. Further studies in this direction are currently under way.

## Acknowledgements

F.G. is grateful to Dr M. Urbano, Prof. C. Castiglioni and Dr D. Fazzi for useful discussions.

## Notes and references

1 (a) A. J. Heeger, N. S. Sariciftci and E. B. Namdas, *Semiconducting and Metallic Polymers*, Oxford University

Press, 2010; (b) H. Klauk, *Organic Electronics: Materials, Manufacturing and Applications*, Wiley-VCH, Weinheim, Germany, 2006; (c) Z. Bao and J. Locklin, *Organic Field-Effect Transistors*, CRC Press, 2007; (d) C.-A. Di, F. Zhang and D. Zhu, *Adv. Mater.*, 2013, **25**, 313–330.

- 2 (a) P. M. Beaujuge, H.-N. Tsao, M. R. Hansen, C. M. Amb, C. Risko, J. Subbiah, R. K. Choudhury, A. Mavrinskiy, W. Pisula, J.-L. Brédas, F. So, K. Müllen and J. R. Reynolds, *J. Am. Chem. Soc.*, 2012, **134**, 8944–8957; (b) J. Mei, Y. Diao, A. L. Appleton, L. Fang and Z. Bao, *J. Am. Chem. Soc.*, 2013, **135**, 6724–6742.
- 3 (a) J. Mei, D. H. Kim, A. L. Ayzner, M. F. Toney and Z. Bao, *J. Am. Chem. Soc.*, 2011, **133**, 20130–20133; (b) K. Takimiya, H. Ebata, K. Sakamoto, T. Izawa, T. Otsubo and Y. Kunugi, *J. Am. Chem. Soc.*, 2006, **128**, 12604–12605; (c) J. Li, Y. Zhao, H. S. Tan, Y. L. Guo, C.-A. Di, G. Yu, Y. Q. Liu, M. Lin, S. H. Lim, Y. H. Zhou, H. B. Su and B. S. Ong, *Sci. Rep.*, 2012, **2**, 754.
- 4 C. Wang, H. Dong, W. Hu, Y. Liu and D. Zhu, *Chem. Rev.*, 2012, **112**, 2208–2267.
- 5 S. Holliday, J. E. Donaghey and I. McCulloch, *Chem. Mater.*, 2014, **26**, 647–663.
- 6 (a) H. Minemawari, T. Yamada, H. Matsui, J. Tsutsumi, S. Haas, R. Chiba, R. Kumai and T. Hasegawa, *Nature*, 2011, **475**, 364–367; (b) H. Ebata, T. Izawa, E. Miyazaki, K. Takimiya, M. Ikeda, H. Kuwabara and T. Yui, *J. Am. Chem. Soc.*, 2007, **129**, 15732–15733.
- 7 A. Y. Amin, A. Khassanov, K. Reuter, T. Meyer-Friedrichsen and M. Halik, *J. Am. Chem. Soc.*, 2012, **134**, 16548–16550.
- 8 J. E. Anthony, A. Facchetti, M. Heeney, S. R. Marder and X. W. Zhan, *Adv. Mater.*, 2010, **22**, 3876–3892.
- 9 (a) K. Oniwa, T. Kanagasekaran, T. Jin, Md. Akhtaruzzaman, Y. Yamamoto, H. Tamura, I. Hamada, H. Shimotani, N. Asao, S. Ikeda and K. Tanigaki, *J. Mater. Chem. C*, 2013, **1**, 4163–4170; (b) A. R. Mohebbi, J. Yuen, J. Fan, C. Munoz, M. F. Wang, R. S. Shirazi, J. Seifert and F. Wudl, *Adv. Mater.*, 2011, **23**, 4644–4648; (c) X. G. Guo, F. S. Kim, M. J. Seger, S. A. Jenekhe and M. D. Watson, *Chem. Mater.*, 2012, **24**, 1434–1442; (d) D. T. Chase, A. G. Fix, S. J. Kang, B. D. Rose, C. D. Weber, Y. Zhong, L. N. Zakharov, M. C. Lonergan, C. Nuckolls and M. M. Haley, *J. Am. Chem. Soc.*, 2012, **134**, 10349–10352; (e) R. P. Ortiz, H. Herrera, C. Seoane, J. L. Segura, A. Facchetti and T. J. Marks, *Chem.–Eur. J.*, 2012, **18**, 532–543.
- 10 (a) R. Capelli, S. Toffanin, G. Generali, H. Usta, A. Facchetti and M. Muccini, *Nat. Mater.*, 2010, **9**, 496–503; (b) M. Muccini, *Nat. Mater.*, 2006, **5**, 605–613; (c) J. Zaumseil and H. Sirringhaus, *Chem. Rev.*, 2007, **107**, 1296–1323; (d) J. A. Misewich, R. Martel, P. Avouris, J. C. Tsang, S. Heinze and J. Tersoff, *Science*, 2003, **300**, 783–786.
- 11 Y. Zhao, Y. Guo and Y. Liu, *Adv. Mater.*, 2013, **25**, 5372–5391.
- 12 (a) H. Tamura, I. Hamada, H. Shang, K. Oniwa, Md. Akhtaruzzaman, T. Jin, N. Asao, Y. Yamamoto, T. Kanagasekaran, H. Shimotani, S. Ikeda and K. Tanigaki, *J. Phys. Chem. C*, 2013, **117**, 8072–8078; (b) T. Sakanoue, M. Yahiro, C. Adachi, H. Uchiuzou, T. Takahashi and A. Toshimitsu, *Appl. Phys. Lett.*, 2007, **90**, 171118; (c)

- R. Capelli, F. Dinelli, S. Toffanin, F. Todescato, M. Murgia, M. Muccini, A. Facchetti and T. J. Marks, *J. Phys. Chem. C*, 2008, **112**, 12993–12999; (d) T. Yamao, Y. Shimizu, K. Terasaki and S. Hotta, *Adv. Mater.*, 2008, **20**, 4109–4112; (e) K. Yamane, H. Yanagi, A. Sawamoto and S. Hotta, *Appl. Phys. Lett.*, 2007, **90**, 162108; (f) T. Oyamada, H. Sasabe, C. Adachi, S. Okuyama, N. Shimoji and K. Matsushige, *Appl. Phys. Lett.*, 2005, **86**, 093505; (g) A. Dadvand, A. G. Moiseev, K. Sawabe, W. H. Sun, B. Djukic, I. Chung, T. Takenobu, F. Rosei and D. F. Perepichka, *Angew. Chem., Int. Ed.*, 2012, **51**, 3837–3841.
- 13 M. Melucci, M. Zambianchi, L. Favaretto, M. Gazzano, A. Zanelli, M. Monari, R. Capelli, S. Troisi, S. Toffanin and M. Muccini, *Chem. Commun.*, 2011, **47**, 11840–11841.
- 14 M. Melucci, L. Favaretto, M. Zambianchi, M. Durso, M. Gazzano, A. Zanelli, M. Monari, M. G. Lobello, F. De Angelis, V. Biondo, G. Generali, S. Troisi, W. Koopman, S. Toffanin, R. Capelli and M. Muccini, *Chem. Mater.*, 2013, **25**, 668–676.
- 15 M. Durso, D. Gentili, C. Bettini, A. Zanelli, M. Cavallini, F. De Angelis, M. G. Lobello, V. Biondo, M. Muccini, R. Capelli and M. Melucci, *Chem. Commun.*, 2013, **49**, 4298–4300.
- 16 M. Durso, C. Bettini, A. Zanelli, M. Gazzano, M. G. Lobello, F. De Angelis, V. Biondo, D. Gentili, R. Capelli, M. Cavallini, S. Toffanin, M. Muccini and M. Melucci, *Org. Electron.*, 2013, **14**, 3089–3097.
- 17 D. Gentili, M. Durso, C. Bettini, I. Manet, M. Gazzano, R. Capelli, M. Muccini, M. Melucci and M. Cavallini, *Sci. Rep.*, 2013, **3**, 2581.
- 18 (a) J. Liu, Y. Zhang, H. Phan, A. Sharenko, P. Moonsin, B. Walker, V. Promarak and T.-Q. Nguyen, *Adv. Mater.*, 2013, **25**, 3645–3650; (b) T. Takahashi, S. Li, W. Y. Huang, F. Z. Kong, K. Nakajima, B. J. Shen, T. Ohe and K. Kanno, *J. Org. Chem.*, 2006, **71**, 7967–7977; (c) Q. Miao, X. L. Chi, S. X. Xiao, R. Zeis, M. Lefenfeld, T. Siegrist, M. L. Steigerwald and C. Nuckolls, *J. Am. Chem. Soc.*, 2006, **128**, 1340–1345; (d) J. E. Anthony, D. L. Eaton and S. R. Parkin, *Org. Lett.*, 2002, **4**, 15–18; (e) M. D. Curtis, J. Cao and J. W. Kampf, *J. Am. Chem. Soc.*, 2004, **126**, 4318–4328; (f) M. Halik, H. Klauk, U. Zschieschang, G. Schimid, W. Radlik, S. Ponomarenko, S. Kirchmeyer and W. Weber, *J. Appl. Phys.*, 2003, **93**, 2977–2981; (g) A. J. Lovinger, H. E. Katz and A. Dodabalapur, *Chem. Mater.*, 1998, **10**, 3275–3277; (h) A. Kreyes, A. Mourran, Z. H. Hong, J. B. Wang, M. Möller, F. Gholamrezaie, W. S. C. Roelofs, D. M. de Leeuw and U. Ziener, *Chem. Mater.*, 2013, **25**, 2128–2136; (i) H. B. Akkerman, S. C. B. Mannsfeld, A. P. Kaushik, E. Verploegen, L. Burnier, A. P. Zoombelt, J. D. Saathoff, S. Hong, S. Atahan-Evrenk, X. Liu, A. Aspuru-Guzik, M. F. Toney, P. Clancy and Z. Bao, *J. Am. Chem. Soc.*, 2013, **135**, 11006–11014.
- 19 (a) A. D. Becke, *J. Chem. Phys.*, 1993, **98**, 5648–5652; (b) C. Lee, W. Yang and R. G. Parr, *Phys. Rev. B: Condens. Matter Mater. Phys.*, 1988, **37**, 785–789.
- 20 (a) R. Dovesi, R. Orlando, B. Civalleri, C. Roetti, V. R. Saunders and C. M. Z. Zicovich-Wilson, *Kristallografiya*, 2005, **220**, 571–573; (b) R. Dovesi, V. R. Saunders, C. Roetti, R. Orlando, C. M. Zicovich-Wilson, F. Pascale, B. Civalleri, K. Doll, N. M. Harrison, I. J. Bush, P. D'Arco and M. Llunell, *CRYSTAL09 (CRYSTAL09 User's Manual)*, University of Torino, Torino, 2009.
- 21 M. Corno, C. Busco, B. Civalleri and P. Ugliengo, *Phys. Chem. Chem. Phys.*, 2006, **8**, 2464–2472.
- 22 C. Gatti, V. R. Saunders and C. Roetti, *J. Chem. Phys.*, 1994, **101**, 10686–10696.
- 23 M. A. Spackman and A. S. Mitchell, *Phys. Chem. Chem. Phys.*, 2001, **3**, 1518–1523.
- 24 V. Maslyuk, C. Tegenkamp, H. Pfnur and T. Bredow, *ChemPhysChem*, 2006, **7**, 1055–1061.
- 25 S. J. Grimme, *J. Comput. Chem.*, 2006, **27**, 1787–1799.
- 26 (a) A. Troisi, *Chem. Soc. Rev.*, 2011, **40**, 2347–2358; (b) J. L. Bredas, D. Beljonne, V. Coropceanu and J. Cornil, *Chem. Rev.*, 2004, **104**, 4971–5004; (c) S. Di Motta, E. Di Donato, F. Negri, G. Orlandi, D. Fazzi and C. Castiglioni, *J. Am. Chem. Soc.*, 2009, **131**, 6591.
- 27 M. Pope, C. E. Swenberg, *Electronic Processes in Organic Crystals and Polymers*, Oxford University Press, New York, 2nd edn, 1999.
- 28 (a) M. Cavallini, *J. Mater. Chem.*, 2009, **19**, 6085–6092; (b) M. Cavallini, M. Facchini, M. Massi and F. Biscarini, *Synth. Met.*, 2004, **146**, 283–286.
- 29 R. D. Deegan, O. Bakajin, T. F. Dupont, G. Huber, S. R. Nagel and T. A. Witten, *Nature*, 1997, **389**, 827–829.
- 30 DFT results, however, show that the *anti*-conformer is energetically favored by 1.1 kcal mol<sup>-1</sup> versus the *syn*-conformer. This energy difference may be overcome by crystal packing effects (cohesion energy for crystal structure  $E_{\text{coh}} = 19.92$  kJ mol<sup>-1</sup>).
- 31 The powder pattern of C4-NT4N does not correspond to that reported in ref. 13, hence powder and film corresponds to a new polymorph.